CARDIFF UNIVERSITY
PRIFYSGOL CAERDYDD

ORCA – Online Research @ Cardiff

This is an Open Access document downloaded from ORCA, Cardiff University's institutional repository:https://orca.cardiff.ac.uk/id/eprint/102521/

This is the author's version of a work that was submitted to / accepted for publication.

Citation for final published version:

Jang, Jae Hyuck, Kim, Young-Min, He, Qian , Mishra, Rohan, Qiao, Liang, Biegalski, Michael D., Lupini, Andrew R., Pantelides, Sokrates T., Pennycook, Stephen J., Kalinin, Sergei V. and Borisevich, Albina Y. 2017. In situ observation of oxygen vacancy dynamics and ordering in the epitaxial LaCoO3 system. ACS Nano 11 (7) , pp. 6942-6949. 10.1021/acsnano.7b02188

Publishers page: http://dx.doi.org/10.1021/acsnano.7b02188

Please note:
Changes made as a result of publishing processes such as copy-editing, formatting and page numbers may not be reflected in this version. For the definitive version of this publication, please refer to the published source. You are advised to consult the publisher's version if you wish to cite this paper.

This version is being made available in accordance with publisher policies. See http://orca.cf.ac.uk/policies.html for usage policies. Copyright and moral rights for publications made available in ORCA are retained by the copyright holders.

In Situ Observation of Oxygen Vacancy Dynamics and Ordering in the Epitaxial $LaCoO_3$ System

Jae Hyuck Jang,[†,‡] Young-Min Kim,[†,§,∥] Qian He,[†] Rohan Mishra,[⊥] Liang Qiao,[#] Michael D. Biegalski,[#] Andrew R. Lupini,[†] Sokrates T. Pantelides,[¶] Stephen J. Pennycook,[△] Sergei V. Kalinin,[#] and Albina Y. Borisevich[*,†]

[†]Materials Science and Technology Division, Oak Ridge National Laboratory, Oak Ridge, Tennessee 37831, United States [‡]Center for Electron Microscopy Research, Kore Basic Science Institute, Daejeon 34133, South Korea

[§]Center for Integrated Nanostructure Physics, Institute for Basic Science (IBS), Suwon 16419, Republic of Korea

[∥]Department of Energy Science, Sungkyunkwan University (SKKU), Suwon 16419, Republic of Korea

[⊥]Department of Mechanical Engineering and Materials Science, Washington University in St. Louis, St. Louis, Missouri 63130, United States

[#]Center for Nanophase Materials Sciences, Oak Ridge National Laboratory, Oak Ridge, Tennessee 37831, United States [¶]Department of Physics and Astronomy, Vanderbilt University, Nashville, Tennessee 37235, United States

[△]Department of Materials Science and Engineering, National University of Singapore, 117575, Singapore

* Supporting Information

ABSTRACT: Vacancy dynamics and ordering underpin the electrochemical functionality of complex oxides and strongly couple to their physical properties. In the field of the epitaxial thin films, where connection between chemistry and film properties can be most clearly revealed, the effects related to oxygen vacancies are attracting increasing attention. In this article, we report a direct, real-time, atomic level observation of the formation of oxygen vacancies in the epitaxial $LaCoO_3$ thin films and heterostructures under the influence of the electron beam utilizing scanning transmission electron microscopy (STEM). In the case of $LaCoO_3/SrTiO_3$ superlattice, the formation of the oxygen vacancies is shown to produce quantifiable changes in the interatomic distances, as well as qualitative changes in the symmetry of the Co sites manifested as off-center displacements. The onset of these changes was observed in both the $[100]_{pc}$ and $[110]_{pc}$ orientations in real time. Additionally, annular bright field images directly show the formation of oxygen vacancy channels along [110]pc direction. In the case of 15 u.c. $LaCoO_3$ thin film, we observe the sequence of events during beam-induced formation of oxygen vacancy ordered phases and find them consistent with similar processes in the bulk. Moreover, we record the dynamics of the nucleation, growth, and defect interaction at the atomic scale as these transformations happen. These results demonstrate that we can track dynamic oxygen vacancy behavior with STEM, generating atomic-level quantitative information on phase transformation and oxygen diffusion.

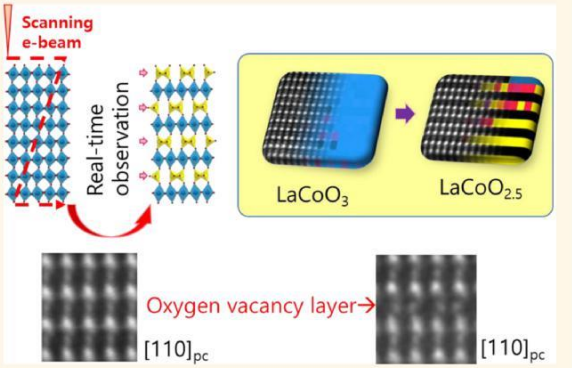

KEYWORDS: oxygen vacancy ordering, vacancy dynamics, lattice dynamics, real-time observation, cobaltite

Physical and electrochemical functionalities of transition metal oxides are intrinsically controlled by the static and dynamic behavior of oxygen vacancies.[1−4] Oxygen stoichiometry controls the oxidation state of the transition metal and affects molar volume and hence bond lengths and bound angles.[5] Additionally, ordering of oxygen vacancies interferes with the intrinsic symmetry of ferroic distortions, enhancing primary lattice instabilities, giving rise to morphotropic-like structures and vacancy-induced polar behavior.[6−8] The confluence of these effects can give rise to structural and

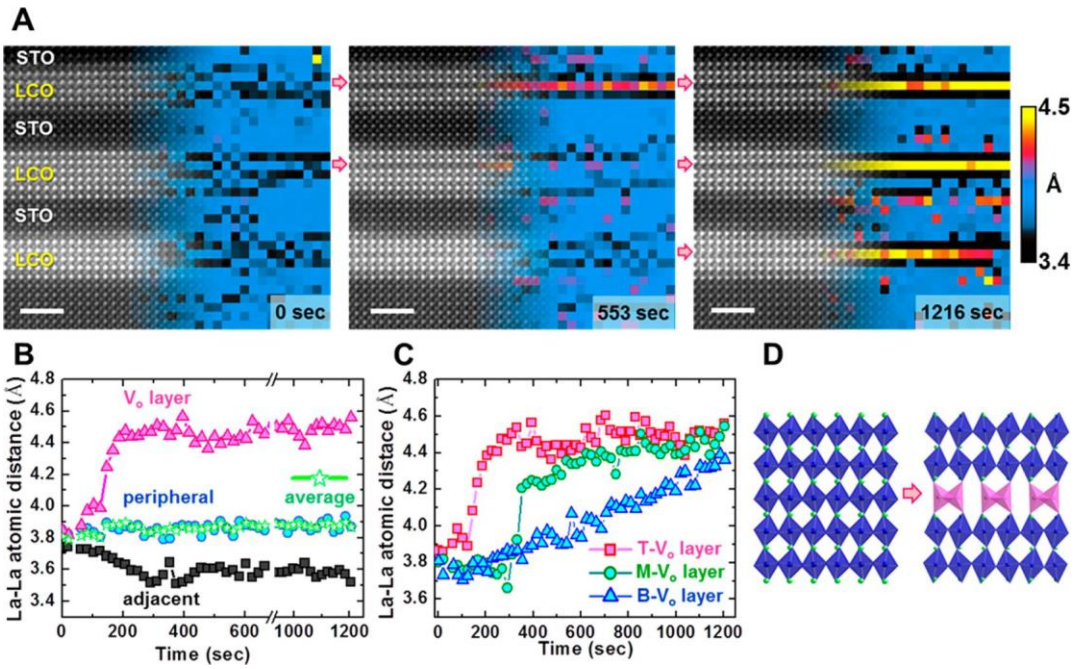

Figure 1. Beam-induced oxygen vacancy ordering in $LaCoO_3/SrTiO_3$ superlattice on $SrTiO_3$ substrate along [100] direction. (A) Sequential ADF images of LCO/STO 3 × 3 structure on STO before/after beam exposure overlaid with the corresponding maps of the out-of-plane interatomic La−La spacings (see text). (B) Average spacings in the central V_O layer (red curve), adjacent (black curve), and peripheral (blue curve) layers within the top LCO block as a function of time; green (star) curve gives the overall average, suggesting that the beam primarily induces redistribution of existing vacancies rather than vacancy injection. (C) Comparison of the evolution of interatomic spacings in the oxygen depleted planes of the top (T), middle (M), and bottom (B) $LaCoO_3$ blocks; the difference are attributed to differences in thickness due to the wedge geometry of the sample. (D) Atomic model of the ordering transition; La atoms are shown in green, CoO_6 octahedra in blue, and CoO_4 tetrahedra in purple. Scale bars are 2 nm.

metal−insulator transitions and also modify magnetic and electronic transport properties.[2,5,9]

Similarly, the formation and dynamics of oxygen vacancies directly control the electrochemical functionality of oxides in applications, such as solid oxide fuel cells, electrolyte membranes, and oxygen sensors.[10−12] Interestingly, many recent results illustrate that reversible vacancy redistribution in oxides is possible at room temperature and below in sufficiently high electric fields.[13−15] These studies, many of which emerged in the last several years, suggest that static and dynamic oxygen vacancy behavior is crucial for understanding the physical functionalities of oxides.[4] Emergent applications such as electroresistive memories,[16] memristive systems,[17] electrochromic devices,[18] as well as recently suggested ionically controlled magnetic structures,[19] illustrate the range of practical applications for these phenomena.

The recognized roles of vacancies in bulk oxide functionalities have been extensively explored in the context of bulk electrochemical and scattering studies.[1,2] Locally, the dual role of vacancies as charge and disclination centers leads to nontrivial behavior in the vicinity of structural defects and interfaces. Recently, these have become accessible to electron microscopy studies through observation of ordering patterns, chemical expansivity-induced lattice strains, changes in oxidation states, or marker cations. In particular, studies of systems, such as $La_{1-x}Sr_xCoO_{2.5}$, $La_{1-x}Sr_xMnO_{2.5}$,[20−22] and others,[23−25] have demonstrated that oxygen depleted planes in the vacancy ordered structures are characterized by darker contrast compared to the planes that are closer to stoichiometric; therefore an ordered vacancy distribution can be easily distinguished from a disordered one. Recently, Kim et al.[26] have demonstrated that for $La_{0.5}Sr_{0.5}CoO_{3-\delta}$ thin films chemical expansivity can be extrapolated down to the atomic level, with the interatomic spacing of an individual layer linearly related to local vacancy content. However, while static structures can be evaluated at the atomic level using multiple approaches, transport and dynamics at the atomic level have so far been inaccessible to local experimental studies, and only theoretical[27,28] and macroscopically averaged investigations have been reported.[29]

Here, we demonstrate that the same level of advanced characterization is possible for the dynamic behavior of oxygen vacancies, and phenomena, such as crystallization of a vacancy-ordered phase, dynamics of the antiphase boundary, and ordered structure evolution, can be observed in real time on an atomic level. Specifically, we explore vacancy (V_O) dynamics using two model systems: one with spatially confined areas of an oxygen conducting material, namely $LaCoO_3/SrTiO_3$ (5 u.c. LCO/5 u.c. STO) superlattice, and one where the oxygen conducting material is not confined, namely 6 nm thick (15 u.c.) $LaCoO_3$ film on a LSAT substrate. We observe structure parameter changes as a function of the electron beam exposure, as well as direct changes in the column occupancies. These studies are enabled through direct, time-resolved observation of interatomic distances, oxygen and cation sublattice distortions, and lattice occupancies on a single unit cell level.

RESULTS AND DISCUSSION

High angle annular dark-field (HAADF) scanning transmission electron microscopy (STEM) images of the superlattice were taken along the pseudocubic [100] direction (Figure 1A). In this imaging mode, atomic columns with higher atomic number

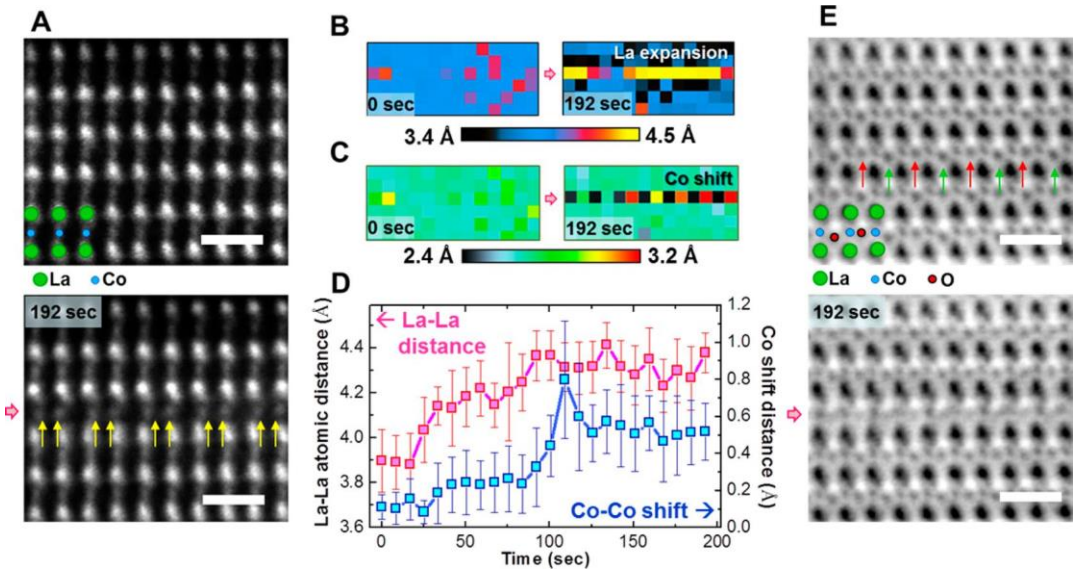

Figure 2. Beam induced V_O ordering in LCO observed down the [110] direction. (A) ADF images before and after exposure showing lattice expansion (La−La) as well as in-plane shifts (Co−Co: yellow arrows). (B),(C) Atomic position maps for La−La out-of-plane spacings and Co−Co in-plane shift derived from images in A. (D) Averages of La−La spacing and differential of Co−Co distances plotted as a function of time, showing that two distortions occur concurrently. (E) Simultaneously acquired ABF images visualizing the O columns in the LCO layer. Before beam exposure there are two types of O columns (red and green arrows), while after beam exposure, oxygen columns are not observed (more details in Figure S2). Scale bars represent 0.5 nm.

Z appear brighter (approximately proportional to Z^2)[30] and so the three brighter LCO blocks can be clearly seen between the dimmer STO layers. Thickness measurements via low-loss electron energy loss spectroscopy show that the sample has a wedge-type geometry, with thickness in the beam direction varying from ~11 nm for the outermost LCO block to ~18 nm for the innermost one (Figure S1). The three images in Figure 1A were taken at different times during a continuous beam exposure experiment. To get quantitative insight into beam-induced changes, we also use the HAADF images to determine the positions of the atomic columns; this approach to aberration-corrected image analysis has emerged in the past few years (see, e.g. refs 31−35) and can give precisions as fine as 4 pm in STEM.[26] The atomic positions are used to calculate lattice spacings in every unit cell. The resulting lattice spacing maps (where each pixel corresponds to one unit cell) are overlaid with the respective images in Figure 1A.

Comparing the three HAADF images, it can be seen that, while the initial contrast inside the LCO blocks is uniform, the prolonged exposure to the electron beam over >20 min (1170 scans) leads to the appearance of dark planes in the middle of each block. The changes are even starker in the lattice spacing maps: in the initial state, we see only a small variation from LCO to STO, reflecting the difference in the respective lattice parameters. In the intermediate and final stages, considerable variation is observed within the LCO blocks. The brightest layers in the lattice spacing maps show the areas of largest lattice expansion and coincide with the dark planes in the HAADF images. Comparison with previous studies of this and other perovskite systems allows us to interpret dark/expanded planes as planes with increased vacancy concentration. The STO layers evidently confine vacancy motion to the 5-unit-cell thick $LaCoO_3$ layers, dictating the in-plane character of the ordering. The full sequence of images and maps is given in Movie S1.

Close examination of Figure 1A reveals several other patterns. The ordering appears to proceed the fastest in the top LCO block (T-LCO), and progressively slower in the middle (M-LCO) and the bottom (B-LCO) blocks. Addition-ally, before the final ordered state is established, the LCO blocks often show lateral inhomogeneities in vacancy distribution; for example, the vacancy ordered state in the M-LCO is propagating from the left to the right side in Movie S1. This behavior is consistent with a nucleation and growth scenario, classical behavior for nucleation controlled first-order transitions.

The observed phenomena can be ascribed to either beam-induced reduction of the material (creation of vacancies), or ordering of preexisting vacancies. In any 5-unit cell LCO block, the central layer (layer 3) appears to accumulate vacancies, and other layers behave depending on the proximity to the central layer. We will heretofore refer to the layers adjacent to the center (layers 2 and 4) as the “adjacent layers”, and the layers 1 and 5 as the “peripheral layers”. To gain insight into the nature of the observed transformations, we quantitatively examine the evolution of the lattice spacings in the T-LCO block, averaging over the central layer (red curve), two adjacent layers (black curve), and two peripheral layers (blue curve) separately; the green curve (star) gives the average over the whole block in Figure 1B. Since lattice spacings in these materials are linearly dependent on oxygen stoichiometry,[1,26,36] this will allow us to see the changes in the total vacancy content as well as its distribution. Figure 1B shows that the average spacing changes very little: from 3.80 to 3.87 Å. The average spacing in the central LCO layer gradually increases and then saturates at 4.48 Å, indicating oxygen depletion, while the average spacing in the two adjacent layers decrease and saturate at 3.58 Å, indicating oxygen enrichment compared to the initial state. These spacing values are very close to those observed for fully tetrahedral (CoO) and fully octahedral (CoO_2) layers, respectively, in brownmillerite polytypes $La_2Co_2O_5$ and $La_3Co_3O_8$.[37,38] The

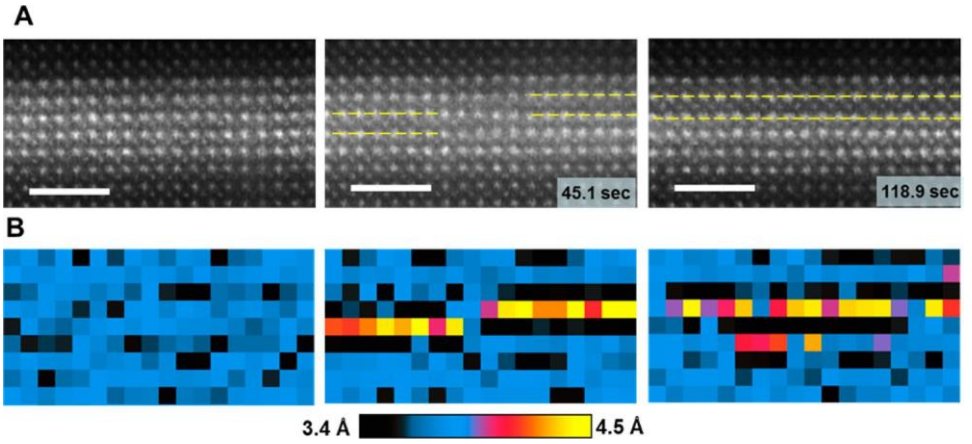

Figure 3. Formation and annealing of antiphase-type defects during beam exposure. (A) Sequential ADF images and (B) corresponding maps of out-of-plane interatomic La−La distances showing evolution of V_O nucleation with a 1 unit cell step/defect along the out-of-plane direction and then subsequent dissolution of the defect. Scale bars are 2 nm.

average spacing in the two peripheral layers stays constant at 3.86 Å. Given linear behavior of spacing with respect to composition, these observations suggest that (a) in the initial state before electron beam exposure, the LCO in the LCO/ STO superlattice contains a substantial amount of vacancies, with an overall composition around $LaCoO_{2.76}$ (8% vacancies), and (b) the impact of the electron beam is primarily in rearrangement and ordering of these existing vacancies, with a very small contribution from vacancy injection. A schematic of the structural transformation happening during vacancy order-ing is given in Figure 1D.

Figure 1C compares the time dependence of the average spacings in the middle (oxygen-depleted) layer of the three LCO blocks. While the starting lattice spacing is the same, and the data almost converge to the same final spacing, corresponding to the CoO stoichiometry, the time scales vary by a factor of 12. We believe that this behavior is primarily driven by the differences in thickness and can be explained by considering the most likely mechanism of the beam-induced changes, namely knock-on interaction of the electrons with the oxygen atoms in the lattice. In a zone axis crystal, the intensity seen by any atom site is strongly affected by the channeling of the probe along the atomic columns. For a very similar $LaMnO_3$ crystal, it was calculated that the O atoms located in the Mn/O columns feel a peak electron concentration enhanced by a factor of 5 relative to the incident probe intensity, within about 5 nm of the entrance surface, whereas the atoms in the pure O columns see only a 2-fold enhancement over about 10 nm.[39] Hence in the thinner crystals the knock on damage rates can be significantly enhanced.

To get further insight into the structural changes accompanying vacancy redistribution, beam-induced ordering was also studied in the [110] pseudocubic orientation. This orientation allows us to observe details of the structure of brownmillerite-like oxygen depleted layers, such as 1D vacancy channels[40] and Co displacements, due to the formation of tetrahedral CoO_4 units.[41] Additionally, in the [110] pseudo-cubic direction oxygen octahedral tilts in the perovskite-like layers can be visualized.[40] These observations will allow us to study if different structural distortions happen gradually or abruptly, and whether different distortions happen simulta-neously. Additionally, close examination of the structure of the oxygen depleted planes will potentially enable us to confirm the saturation composition of the layer.

Representative HAADF images taken before and after sustained electron beam exposure are given in Figure 2A. La−La spacing increases in the middle LCO layer, similar to the observations in the [100] direction, can be clearly seen in the map in Figure 2B; the changes happen on a similar time scale. In addition to the La sublattice changes, in the final state we can also see brownmillerite-like changes in Co positions (indicated by arrows in the HAADF image): Co columns shift laterally in alternating directions, forming pairs inside the depleted plane (a map of in-plane Co shifts is given in Figure 2C). The final difference between larger and smaller Co−Co distances is 0.52 ± 0.15 Å. Figure 2D shows the time dependence of both the La−La spacing and average Co shift; the two parameters follow the same approximate profile, suggesting that these changes are simultaneous.

Further evidence for a fully tetrahedral depleted plane can be obtained from the examination of the simultaneously acquired annular bright field (ABF) images (Figure 2E); ABF images can visualize oxygen columns along with those of cations. In the middle layer of the LCO block in the initial state two distinct types of oxygen columns can be seen, one displaced slightly above and one slightly below the cation plane due to octahedral tilts. In the final state, however, the oxygen column contrast in the depleted layer is gone, while it is still present in the perovskite-like blocks, which is consistent with a fully tetrahedral brownmillerite layer where oxygen columns overlap with Co in the [110] pseudocubic projection. At intermediate stages of the experiment, we see that the oxygen columns above the cation plane disappear first, while the oxygen columns below the cation plane are still present in the depleted layer (see Figure S3). This result is consistent with a recent computational study showing that oxygen vacancies are energetically more stable in the position above the cation plane.[42]

The observations in Figures 1 and 2 illustrate that the e-beam irradiation of the LCO/STO superlattice leads to ordering of pre-existing oxygen vacancies in LCO into (001) planes (or, more precisely, [110] channels within those planes) with a small contribution from vacancy injection. Concurrent changes in La−La spacings, Co−Co spacings, and population of oxygen sublattice suggest that this process should be understood as the

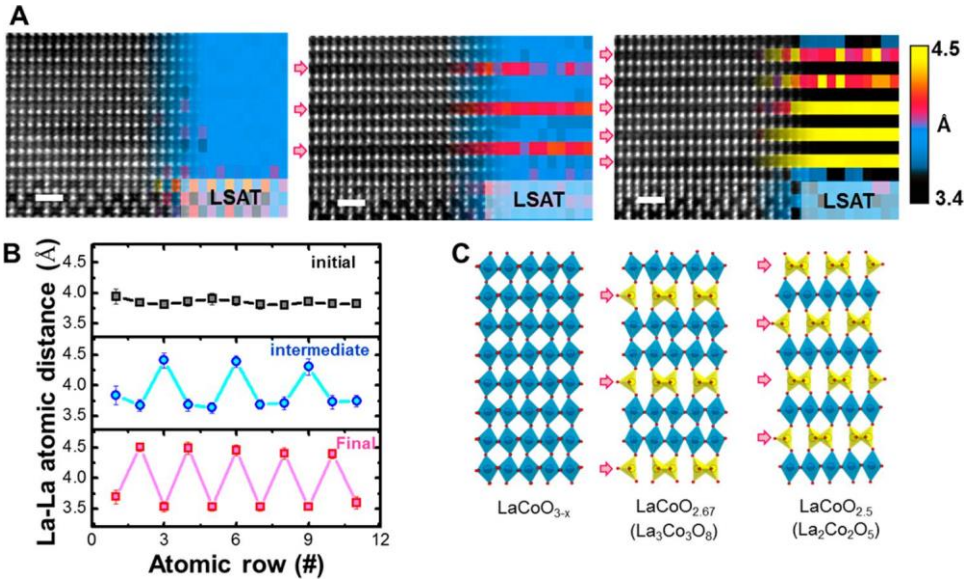

Figure 4. Beam-induced changes in 6 nm $LaCoO_{3-x}$ films on LSAT substrate observed down the [110] direction. (A) Sequential ADF images and the corresponding La−La spacing maps showing the evolution of the structure from a slightly oxygen-deficient uniform perovskite matrix to 2:1, and later 1:1, brownmillerite structures. (B) Profiles of La−La spacing maps for different stages of the beam exposure experiment, clearly showing the emergence of 2:1 and then 1:1 periodicity. (C) The atomic models for the $LaCoO_{3-x}$, $LaCoO_{2.67}$, and brownmillerite $LaCoO_{2.5}$ phases reported during reduction of bulk LCO.[37,38] Scales bars are 1 nm.

nucleation of 1 u.c. thick tetrahedral CoO layers in the perovskite matrix containing a significant concentration of oxygen vacancies. The time-resolved measurements allow the kinetics of this process to be quantified and suggest first-order type kinetics with a distinct nucleation phase and subsequent lateral growth.

These studies can be expanded further to observe the interactions of nuclei formed at different locations. An example of such an observation is shown in Figure 3, illustrating formation of two distinct brownmillerite nuclei shifted vertically by 1 u.c. with respect to each other. This kink in the vacancy plane is effectively a segment of antiphase boundary, and is thus associated with increased energy. As more energy is being pumped into the system with additional beam exposure, the kink disappears: the brownmillerite nucleus on the left splits the originally depleted plane in two, and the final state has two oxygen depleted planes, each with a lower population of oxygen vacancies than the original one, but no antiphase boundaries.

These observations directly reveal the atomic-level mechanisms underlying macroscopic electrochemical behaviors in these systems. For example, Chen et al.[43] have shown that the expansion due to reduction of LSCO bulk materials shows "hysteresis behavior", including rapid expansion upon a change of P_{O2} with subsequent slow secondary relaxation. Our in situ V_O ordering experiments demonstrate different stages of vacancy transport and provide a framework for quantitative kinetic studies with single unit-cell resolution.

To illustrate this possibility, we conduct a similar experiment on LCO films on LSAT substrates; due to epitaxial strain conditions,[24,44] vacancy ordering in this case is also in-plane, providing a good comparison with the superlattice case. Figure 4A shows a set of HAADF images of different stages of the beam exposure experiment, overlaid with the corresponding out-of-plane La−La spacing maps. Similar to the superlattice case, the ordered arrangement is quickly established. However, unlike the superlattice case, the ordered arrangement is first established as a 2:1 brownmillerite polytype (with 2 u.c. perovskite blocks), and later converts into 1:1 brownmillerite; these changes are clearly visible in the lattice parameter maps of the images (Figure 4A) and map profiles given in Figure 4B. This evolution is strongly reminiscent of the sequence of transformations when bulk LCO is reduced, first forming $LaCoO_{2.67}$ and then $LaCoO_{2.5}$ (see schematic in Figure 4C).[37,38] The newly generated oxygen vacancies appear to travel mostly in horizontal direction (parallel to the substrate), and sometimes also in the vertical direction, as shown in Figure 3. We are currently using this information to investigate the energetics of the oxygen vacancy motion using density functional theory (DFT) calculations. We are further planning to use DFT findings to enable the control of the direction of oxygen vacancy transport using electron beam (Figure S3).

This work represents a significant step forward with respect to existing literature. Previously, the ability to image and quantify static oxygen vacancies in defective perovskites was demonstrated. In this article we observe dynamic behavior of oxygen vacancies as they migrate and form under the influence of the electron beam, with atomic resolution and in real time. The comparatively small electron probe current in STEM mode (~pA), coupled with typical dwell time per pixel of just 4−6 μs, provides for the ideal combination of our observation speed and the process speed, conditions that would be harder to achieve using much higher beam current or (nonscanning) TEM mode. STEM allows us to directly observe and quantify the lattice changes due to the oxygen vacancy formation, as well as dynamic interplay between layers with different oxygen vacancy concentrations (see Figures 3 and 4). While previously reported results were very useful for refining the predictions for the energetics of vacancy formation and oxygen diffusion in different crystallographic directions, this article takes us a few steps closer to directly observing ion diffusion paths in their full complexity.

CONCLUSION

We have demonstrated that vacancy dynamics and ordering in oxides can be tracked quantitatively at the single column level through observation of interatomic strains. Here, we observe the effect of the collective motion of oxygen vacancies on the underlying lattice with atomic resolution, rather than single oxygen vacancy effect. Our in situ observations demonstrate nucleation of vacancy ordered planes, dynamics of antiphase boundaries, and energy-driven splitting of the oxygen vacancy planes. Furthermore, observations of Co−Co pairing confirm the formation of brownmillerite from vacancy-ordered perovskite, allowing solid-state reaction pathways to be separated on a single unit-cell level. The concomitant changes in the Co−O−Co bond length are also visualized at the atomic scale. We have observed dynamically the lateral propagation of a vacancy plane from the nucleation site, as well as interaction of the two vacancy planes to form brownmillerite structure via vertical transport. Crucially, the processes we observe follow the same general sequence of events as seen in bulk phase trans-formations, suggesting that electron beam does not fundamen-tally change energy landscape of the system but rather alleviates some of the energy barriers.

METHODS

Thin Film Synthesis and STEM Sample Preparation. The $LaCoO_3/SrTiO_3$ superlattices and $LaCoO_3$ thin films were grown on $SrTiO_3$ and $La_{0.3}Sr_{0.7}Al_{0.65}Ta_{0.35}O_3$ (LSAT) substrates, respectively, by pulsed laser deposition under identical processing conditions with 200 mTorr O_2 at 650 °C and maintained with 200 Torr O_2 gas down to room temperature. Film growth was monitored with in situ RHEED. Prior to deposition, $SrTiO_3$ substrates were subjected to the typical HF-etch process and subsequent anneal at 1000 °C for 2 h to get the atomically flat TiO_2-terminated surface. LSAT substrates are annealed at 1000 °C for 2 h to improve the surface quality. Samples for STEM analysis were prepared in cross sections oriented along the 100 and 110 pseudocubic directions using precision polishing followed by Ar ion milling.

STEM Imaging and Analysis. Aberration corrected STEM images were recorded using Nion UltraSTEM 200, operated at 200 kV and equipped with a Gatan Enfinium electron energy loss spectrometer (used for collecting thickness information in Figure S1). To perform in situ observation of oxygen vacancy ordering, we collected the sequential images via continued scans of the regions of interest in $LaCoO_3$ film or superlattice. The details of scanning conditions for data sets corresponding to each figure are given in the Table S1. Regardless of the zone axis orientation of the LCO/STO superlattice sample, similar behavior was observed (see Movie S1 and Movie S3). Moreover, vacancy ordering was also observed using a 100 kV Nion UltraSTEM under similar scanning conditions. Atom coordinates were determined via center-of-mass refinement method; see more details in Supporting Information.

ASSOCIATED CONTENT

Details of experimental conditions for dynamic STEM imagaing, EELS thickness measurement of V_O ordering region, vacancy ordering dynamics, direct observations of oxygen vacancy channels via ABF images, ADF images before/after beam exposure along $[110]_{pc}$, and real-time phase transformation by electron beam (PDF)

Movie of the inhomogeneity of V_O ordering in M-LCO layer and propagation from left to right side (AVI)

Movie of atomic position maps of La-La spacing corresponding to Movie S1(AVI)

Movie of lattice dynamics of La and Co columns due to V_O ordering in $LaCoO_3/SrTiO_3$ superlattice along $[110]_{pc}$ direction (AVI)

Movie of ADF/ABF images of vacancy ordering in $LaCoO_3/SrTiO_3$ superlattice along $[110]_{pc}$ (AVI)

Movie of lattice dynamic of La and Co columns due to V_O ordering corresponding to Movie S4 (AVI)

Movie of direct observation of vacancy ordering channels in $LaCoO_3$ (AVI)

Movie of ADF image and atomic position map showing the formation of depleted layer kink in LCO block (AVI)

AUTHOR INFORMATION

Corresponding Author

*albinab@ornl.gov.

ORCID

Jae Hyuck Jang: 0000-0002-9133-3286

Rohan Mishra: 0000-0003-1261-0087

Albina Y. Borisevich: 0000-0002-3953-8460

Author Contributions

J.H.J. and A.Y.B. conceived and designed the in situ experiments, J.H.J. carried out in situ experiments and collected the STEM data, Y-M.K. and Q.H. contributed to data analysis. A.R.L. developed scripts for sequential data acquisition and alignment. L.Q. and M.D.B grew the sample, R.M. and S.T.P performed the DFT calculations. A.Y.B. and S.V.K. coordinated and led the project. All authors contributed to writing the paper.

Notes

The authors declare no competing financial interest.

ACKNOWLEDGMENTS

Research supported (J.H.J., Q.H., A.R.L., A.Y.B, S.V.K.) by the U.S. Department of Energy (DOE), Basic Energy Sciences (BES), Materials Sciences and Engineering Division, by (L.Q. and M.D.B.) Center for Nanophase Materials Sciences, which is supported at ORNL by DOE BES, and through a user project supported by ORNL's Center for Nanophase Materials Sciences (CNMS), which is sponsored by the Scientific User Facilities Division, Office of Basic Energy Sciences, U.S. Department of Energy. Y.M.K. was supported by the Institute for Basic Science (IBS-R011-D1) and Creative Materials Discovery Program through the NRF (National Research Foundation of Korea) grant (NRF-2015M3D1A1070672) in Korea. R.M. and S.T.P. were supported by DOE Grant No. DE-FG02-09ER46554.

REFERENCES

(1) Adler, S. B. Factors Governing Oxygen Reduction in Solid Oxide Fuel Cell Cathodes. Chem. Rev. 2004, 104, 4791−4843.

(2) Mitchell, J. F.; Argyriou, D. N.; Potter, C. D.; Hinks, D. G.; Jorgensen, J. D.; Bader, S. D. Structural Phase Diagram of $La_{1-x}Sr_xMnO_{3+\delta}$: Relationship to Magnetic and Transport Properties. Phys. Rev. B: Condens. Matter Mater. Phys. 1996, 54, 6172−6183.

(3) Kalinin, S. V.; Spaldin, N. A. Functional Ion Defects in Transition Metal Oxides. Science 2013, 341, 858−859.

(4) Kalinin, S. V.; Borisevich, A.; Fong, D. Beyond Condensed Matter Physics on The Nanoscale: The Role of Ionic and Electrochemical Phenomena in The Physical Functionalities of Oxide Materials. ACS Nano 2012, 6, 10423−10437.

(5) Imada, M.; Fujimori, A.; Tokura, Y. Metal-Insulator Transitions. Rev. Mod. Phys. 1998, 70, 1039−1263.
(6) Seidel, J.; Luo, W.; Suresha, S. J.; Nguyen, P. K.; Lee, A. S.; Kim, S. Y.; Yang, C. H.; Pennycook, S. J.; Pantelides, S. T.; Scott, J. F.; Ramesh, R. Prominent Electrochromism Through Vacancy-Order Melting in a Complex Oxide. Nat. Commun. 2012, 3, 799.
(7) Young, J.; Moon, E. J.; Mukherjee, D.; Stone, G.; Gopalan, V.; Alem, N.; May, S. J.; Rondinelli, J. M. Polar Oxides without Inversion Symmetry through Vacancy and Chemical Order. J. Am. Chem. Soc. 2017, 139, 2833−2841.
(8) Mishra, R.; Kim, Y. M.; Salafranca, J.; Kim, S. K.; Chang, S. H.; Bhattacharya, A.; Fong, D. D.; Pennycook, S. J.; Pantelides, S. T.; Borisevich, A. Y. Oxygen-Vacancy-Induced Polar Behavior in $(LaFeO_3)_2/(SrFeO_3)$ superlattices. Nano Lett. 2014, 14, 2694−2701.
(9) Mizusaki, J.; Mori, N.; Takai, H.; Yonemura, Y.; Minamiue, H.; Tagawa, H.; Dokiya, M.; Inaba, H.; Naraya, K.; Sasamoto, T.; Hashimoto, T. Oxygen Nonstoichiometry and Defect Equilibrium in the Perovskite-Type Oxides $La_{1-x}Sr_xMnO_{3+d}$. Solid State Ionics 2000, 129, 163−177.
(10) Bagotsky, V. S. Fuel Cells: Problems and Solutions; Wiley, 2009.
(11) Maier, J. Nanoionics: Ion Transport and Electrochemical Storage in Confined Systems. Nat. Mater. 2005, 4, 805−815.
(12) Maier, J. Defect Chemistry - Composition, Transport and Reactions in the Solid-State 2 Kinetics. Angew. Chem., Int. Ed. Engl. 1993, 32, 528−542.
(13) Jiang, W.; Noman, M.; Lu, Y. M.; Bain, J. A.; Salvador, P. A.; Skowronski, M. Mobility of Oxygen Vacancy in SrTiO3 and Its Implications for Oxygen-Migration-Based Resistance Switching. J. Appl. Phys. 2011, 110, 034509.
(14) Yi, H. T.; Choi, T.; Choi, S. G.; Oh, Y. S.; Cheong, S. W. Mechanism of the Switchable Photovoltaic Effect in Ferroelectric $BiFeO_3$. Adv. Mater. 2011, 23, 3403−3407.
(15) Fleig, J.; Schintlmeister, A.; Opitz, A. K.; Hutter, H. The Determination of the Three-Phase Boundary Width of Solid Oxide Fuel Cell Cathodes by Current-Driven ^{18}O Tracer Incorporation. Scr. Mater. 2011, 65, 78−83.
(16) Valov, I.; Waser, R.; Jameson, J. R.; Kozicki, M. N. Electrochemical Metallization Memories-Fundamentals, Applications, Prospects. Nanotechnology 2011, 22, 254003.
(17) Strukov, D. B.; Snider, G. S.; Stewart, D. R.; Williams, R. S. The Missing Memristor Found. Nature 2008, 453, 80−83.
(18) Llordes, A.; Garcia, G.; Gazquez, J.; Milliron, D. J. Tunable Near-Infrared and Visible-Light Transmittance in Nanocrystal-in-Glass Composites. Nature 2013, 500, 323−326.
(19) Bauer, U.; Emori, S.; Beach, G. S. D. Voltage-Controlled Domain Wall Traps in Ferromagnetic Nanowires. Nat. Nanotechnol. 2013, 8, 411−416.
(20) Torija, M. A.; Sharma, M.; Gazquez, J.; Varela, M.; He, C.; Schmitt, J.; Borchers, J. A.; Laver, M.; El-Khatib, S.; Leighton, C. Chemically Driven Nanoscopic Magnetic Phase Separation at the $SrTiO_3$ (001)/$La_{1-x}Sr_xCoO_3$ interface. Adv. Mater. 2011, 23, 2711− 2715.
(21) Ferguson, J. D.; Kim, Y.; Kourkoutis, L. F.; Vodnick, A.; Woll, A. R.; Muller, D. A.; Brock, J. D. Epitaxial Oxygen Getter for a Brownmillerite Phase Transformation in Manganite Films. Adv. Mater. 2011, 23, 1226−1230.
(22) Torija, M. A.; Sharma, M.; Fitzsimmons, M. R.; Varela, M.; Leighton, C. Epitaxial $La_{0.5}Sr_{0.5}CoO_3$ Thin Films: Structure, Magnet-ism, and Transport. J. Appl. Phys. 2008, 104, 023901.
(23) Gazquez, J.; Luo, W.; Oxley, M. P.; Prange, M.; Torija, M. A.; Sharma, M.; Leighton, C.; Pantelides, S. T.; Pennycook, S. J.; Varela, M. Atomic-Resolution Imaging of Spin-State Superlattices in Nano-pockets within Cobaltite Thin Films. Nano Lett. 2011, 11, 973−976.
(24) Klenov, D. O.; Donner, W.; Foran, B.; Stemmer, S. Impact of Stress on Oxygen Vacancy Ordering in Epitaxial $(La_{0.5}Sr_{0.5})CoO_{3-\partial}$ Thin Films. Appl. Phys. Lett. 2003, 82, 3427−3429.
(25) Gspan, C.; Grogger, W.; Bitschnau, B.; Bucher, E.; Sitte, W.; Hofer, F. Crystal Structure of $La_{0.4}Sr_{0.6}CoO_{2.71}$ Investigated by TEM and XRD. J. Solid State Chem. 2008, 181, 2976−2982.
(26) Kim, Y. M.; He, J.; Biegalski, M. D.; Ambaye, H.; Lauter, V.; Christen, H. M.; Pantelides, S. T.; Pennycook, S. J.; Kalinin, S. V.; Borisevich, A. Y. Probing Oxygen Vacancy Concentration and Homogeneity in Solid-Oxide Fuel-Cell Cathode Materials on the Subunit-Cell Level. Nat. Mater. 2012, 11, 888−894.
(27) Chroneos, A.; Yildiz, B.; Tarancon, A.; Parfitt, D.; Kilner, J. A. Oxygen Diffusion in Solid Oxide Fuel Cell Cathode and Electrolyte Materials: Mechanistic Insights from Atomistic Simulations. Energy Environ. Sci. 2011, 4, 2774−2789.
(28) Kendrick, E.; Kendrick, J.; Knight, K. S.; Islam, M. S.; Slater, P. R. Cooperative Mechanisms of Fast-Ion Conduction in Gallium-Based Oxides with Tetrahedral Moieties. Nat. Mater. 2007, 6, 871−875.
(29) Inoue, S.; Kawai, M.; Ichikawa, N.; Kageyama, H.; Paulus, W.; Shimakawa, Y. Anisotropic Oxygen Diffusion at Low Temperature in Perovskite-Structure Iron Oxides. Nat. Chem. 2010, 2, 213−217.
(30) Scanning Transmission Electron Microscopy Imaging and Analysis; Pennycook, S. J. N., Peter, D., Eds.; Springer, 2011.
(31) Jia, C. L.; Mi, S. B.; Faley, M.; Poppe, U.; Schubert, J.; Urban, K. Oxygen Octahedron Reconstruction in the $SrTiO_3/LaAlO_3$ Hetero-interfaces Investigated Using Aberration-Corrected Ultrahigh-Reso-lution Transmission Electron Microscopy. Phys. Rev. B: Condens. Matter Mater. Phys. 2009, 79, 081405.
(32) Jia, C. L.; Mi, S. B.; Urban, K.; Vrejoiu, I.; Alexe, M.; Hesse, D. Atomic-Scale Study of Electric Dipoles Near Charged and Uncharged Domain Walls in Ferroelectric Films. Nat. Mater. 2008, 7, 57−61.
(33) Borisevich, A. Y.; Chang, H. J.; Huijben, M.; Oxley, M. P.; Okamoto, S.; Niranjan, M. K.; Burton, J. D.; Tsymbal, E. Y.; Chu, Y. H.; Yu, P.; Ramesh, R.; Kalinin, S. V.; Pennycook, S. J. Suppression of Octahedral Tilts and Associated Changes in Electronic Properties at Epitaxial Oxide Heterostructure Interfaces. Phys. Rev. Lett. 2010, 105, 087204.
(34) Chang, H. J.; Kalinin, S. V.; Morozovska, A. N.; Huijben, M.; Chu, Y. H.; Yu, P.; Ramesh, R.; Eliseev, E. A.; Svechnikov, G. S.; Pennycook, S. J.; Borisevich, A. Y. Atomically Resolved Mapping of Polarization and Electric Fields Across Ferroelectric/Oxide Interfaces by Z-contrast Imaging. Adv. Mater. 2011, 23, 2474−2479.
(35) Nelson, C. T.; Winchester, B.; Zhang, Y.; Kim, S. J.; Melville, A.; Adamo, C.; Folkman, C. M.; Baek, S. H.; Eom, C. B.; Schlom, D. G.; Chen, L. Q.; Pan, X. Q. Spontaneous Vortex Nanodomain Arrays at Ferroelectric Heterointerfaces. Nano Lett. 2011, 11, 828−834.
(36) Zuev, A. Y.; Sereda, V. V.; Tsvetkov, D. S. Defect Structure and Defect-Induced Expansion of MIEC Oxides: Doped Lanthanum Cobaltites. J. Electrochem. Soc. 2012, 159, F594−F599.
(37) Hansteen, O. H.; Fjellvag, H.; Hauback, B. C. Crystal Structure, Thermal and Magnetic Properties of $La_3Co_3O_8$. Phase Relations for $LaCoO_{3-\delta}$ ($0.00 \leq \delta \leq 0.05$) at 673 K. J. Mater. Chem. 1998, 8, 2081− 2088.
(38) Hansteen, O. H.; Fjellvag, H.; Hauback, B. C. Crystal Structure and Magnetic Properties of $La_2Co_2O_5$. J. Solid State Chem. 1998, 141, 411−417.
(39) Oxley, M. P.; Varela, M.; Pennycook, T. J.; van Benthem, K.; Findlay, S. D.; D'Alfonso, A. J.; Allen, L. J.; Pennycook, S. J. Interpreting Atomic-Resolution Spectroscopic Images. Phys. Rev. B: Condens. Matter Mater. Phys. 2007, 76, 064303.
(40) Parsons, T. G.; D'Hondt, H.; Hadermann, J.; Hayward, M. A. Synthesis and Structural Characterization of $La_{1-x}A_xMnO_{2.5}$(A = Ba, Sr, Ca) Phases: Mapping the Variants of the Brownmillerite Structure. Chem. Mater. 2009, 21, 5527−5538.
(41) Chroneos, A.; Parfitt, D.; Kilner, J. A.; Grimes, R. W. Anisotropic Oxygen Diffusion in Tetragonal $La_2NiO_{4+\delta}$: Molecular Dynamics Calculations. J. Mater. Chem. 2010, 20, 266−270.
(42) Han, J. W.; Yildiz, B. Enhanced One Dimensional Mobility of Oxygen on Strained $LaCoO_3$ (001) surface. J. Mater. Chem. 2011, 21, 18983−18990.
(43) Chen, X.; Yu, J.; Adler, S. B. Thermal and Chemical Expansion of Sr-Doped Lanthanum Cobalt Oxide ($La_{1-x}Sr_xCoO_{3-\delta}$). Chem. Mater. 2005, 17, 4537−4546.
(44) Gazquez, J.; Bose, S.; Sharma, M.; Torija, M. A.; Pennycook, S. J.; Leighton, C.; Varela, M. Lattice Mismatch Accommodation via

Oxygen Vacancy Ordering in Epitaxial $La_{0.5}Sr_{0.5}CoO_{3-\delta}$ Thin Films.
APL Mater. 2013, 1, 012105.